Through the lens of Sgr A*: identifying strongly lensed Continuous Gravitational Waves beyond the Einstein radius

Stefano Savastano,[1,*] Filippo Vernizzi,[2,†] and Miguel Zumalacárregui[1,‡]

[1] *Max Planck Institute for Gravitational Physics (Albert Einstein Institute) Am Mühlenberg 1, D-14476 Potsdam-Golm, Germany*

[2] *Institut de Physique Théorique, Université Paris Saclay CEA, CNRS, 91191 Gif-sur-Yvette, France*

(Dated: January 2, 2023)

Once detected, lensed gravitational waves will afford new means to probe the matter distribution in the universe, complementary to electromagnetic signals. Sources of continuous gravitational waves (CWs) are long-lived and stable, making their lensing signatures synergic to short mergers of compact binaries. CWs emitted by isolated neutron stars and lensed by Sgr A*, the super-massive black hole at the center of our galaxy, might be observable by the next generation of gravitational wave detectors. However, it is unknown under which circumstances these sources can be identified as lensed. Here we show that future detectors can distinguish lensed CWs and measure all parameters with precision $\sim 1-10\%$ for sources within $2-4$ Einstein radii of Sgr A*, depending on the source's distance. Such a detection, which relies on the relative motion of the observer-lens-source system, can be observed for transverse velocities above 3 km/s. Therefore, the chances of observing strongly lensed neutron stars increase by one order of magnitude with respect to previous estimates. Observing strongly lensed CWs will enable novel probes of the galactic center and fundamental physics.

Introduction. Gravitational lensing is the deflection and magnification of light propagating through an inhomogeneous gravitational field, possibly leading to distortion and splitting of the original source into multiple images [1]. It has proven to be a powerful tool in astrophysics and cosmology, for example in the search for dark objects, exploration of the universe's large-scale structure and measurement of cosmological parameters [2, 3].

With the recent rise of gravitational wave (GW) astronomy, the lensing of gravitational waves emitted by coalescing binary black holes (BHs) and neutron stars (NSs) has become the subject of intense research. The coherence, low frequency and frequency evolution of these sources enables the observation of diffraction [4–8] and phase [9–11] effects that are challenging to observe with electromagnetic (EM) waves. While no detection of lensed GWs has yet been made [12–15], the increasing rate of GW observations offers a promising future [16, 17].

In addition to transient signals produced by explosive binary coalescences, detectors can also observe long-lived signals with a much slower frequency evolution: the so-called continuous GWs (CWs). Sources of this type of quasi-monochromatic signals fall into two main categories: 1) stellar-mass binaries well before coalescence, which will be detectable by LISA [18–20], and exotic binaries, such as sub-solar primordial BHs, which can be searched with ground-based detectors [21, 22]; 2) rapidly rotating non-axisymmetric neutron stars with a quadrupolar deformation, which will also be observable by ground-based detectors. These signals have been searched for in the LIGO-Virgo-Kagra (LVK) data [23, 24]; see Refs. [25–28] for reviews.

The lensing of CWs leads to interesting and clear signatures. In particular, due to the coherent nature of GWs, a lens can act on them as a diffractive barrier, inducing interference fringes on the detected signal, if the observer-lens-source system is in relative transverse motion [29, 30]. This is in contrast to EM waves, where the contributions of the different points of the finite-size source add up incoherently, cancelling out the pattern (although some EM sources can avoid this limitation [31–34]). Despite these intriguing possibilities of distinguishing lensed and unlensed CWs, the ability of observations to infer the lens parameters remains an open question.

While no clear detection of CWs has been registered yet, the sheer number of NSs in the Milky Way (MW) galaxy, estimated in $\sim 10^9$ from population synthesis studies [35], suggests that detection of lensed signals is plausible for future observations. (See [36] for an estimate on the total number of NSs probed with current and future detectors.) A recent study [37] estimated that 3G interferometers will be able to observe $\mathcal{O}(1-10)$ strongly lensed signals of rapidly spinning NSs within the Einstein cone of SgrA*, the supermassive black hole at the center of the MW, the precise number depending on their spatial distribution in the MW.

Motivated by such a prospect, in this letter we study the phenomenology of strongly-lensed CWs, the inference of lens parameters and the potential for detection by next-generation GW observatories. For concreteness, we will focus on monochromatic, isolated rotating NS moving at constant velocity and lensed by Sgr A*.

Strong lensing imprints on CWs. Let us briefly recall what the effect of a lens on the GW is; see e.g. [4, 38] for a derivation in the fixed-lens case and App. A for

*Electronic address: stefano.savastano@aei.mpg.de
†Electronic address: filippo.vernizzi@ipht.fr
‡Electronic address: miguel.zumalacarregui@aei.mpg.de

the moving-lens case. We work in the geometric optics limit and denote the observed and true angular position of the source by $\boldsymbol{\theta}_l$ and $\boldsymbol{\theta}_s$, respectively, and the observer-lens, observer-source and lens-source angular-diameter distances by r_l, r_s and r_{ls}, respectively; see Fig. 1.

Given a Fourier mode with frequency f of a lensed and unlensed gravitational wave, respectively $\tilde{h}_l(f)$ and $\tilde{h}_0(f)$, the amplification factor, $F(f) \equiv \tilde{h}_l(f)/\tilde{h}_0(f)$, is given by a sum over images as

$$F(f, \boldsymbol{\theta}_s) = \sum_j |\mu_j(\boldsymbol{\theta}_s)|^{1/2} \exp\left[i2\pi f t_j(\boldsymbol{\theta}_s) - i\pi n_j\right] , \quad (1)$$

where $\mu_j(\boldsymbol{\theta}_s) = \det(\partial\boldsymbol{\theta}_s/\partial\boldsymbol{\theta}_{l,j})^{-1}$ is the magnification and $t_j(\boldsymbol{\theta}_s) = \frac{r_l r_s}{2r_{ls}}|\boldsymbol{\theta}_{l,j} - \boldsymbol{\theta}_s|^2 - \hat{\psi}(\boldsymbol{\theta}_{l,j})$ is the time of arrival of the j-th image (with $\hat{\psi}$ the lensing potential) from the lens to the source, and $n_j = 0, 1/2, 1$ for a minimum, a saddle and a maximum point of t_j, respectively.

The relative transverse motion of the observer-lens-source system also affects the frequency of the lensed gravitational wave. Denoting the transverse velocity of the observer, of the lens and of the source, measured in their respective planes, as $\boldsymbol{v}_o$, $\boldsymbol{v}_l$ and $\boldsymbol{v}_s$ respectively, the *combined effective* transverse velocity in the plane of the lens results in [39]

$$\boldsymbol{v} = \boldsymbol{v}_l - \frac{r_l}{r_s}\boldsymbol{v}_s - \frac{r_{ls}}{r_s}\boldsymbol{v}_o , \quad (2)$$

which we will call the *effective lens velocity* for short, although it should be understood that it can also be due to the movement of the source or of the observer. This motion makes the angular position of the source time dependent: $\dot{\boldsymbol{\theta}}_s = \boldsymbol{v}/r_l$. Consequently, both the magnification $\mu_j(\boldsymbol{\theta}_s)$ and the arrival time $t_j(\boldsymbol{\theta}_s)$ depend on time. The time dependence of the arrival time induces a frequency shift (we set $c = 1$ throughout),

$$\frac{\Delta f_j}{f} = -\dot{t}_j = \boldsymbol{v} \cdot \boldsymbol{\alpha}_j , \quad (3)$$

where $\boldsymbol{\alpha} \equiv \frac{r_s}{r_{ls}}(\boldsymbol{\theta}_l - \boldsymbol{\theta}_s)$ is the deflection angle and the second equality in (3) follows from the definition of the arrival time above and the chain rule for the time derivative. See App. A for more details.

For a strongly lensed system, different images arrive at different times at the detector, where they can mutually interfere and, if the time delay between images is smaller than the in-band time, produce a modulated signal [37]. The intensity of the lensed signal in the frequency domain can be obtained by squaring Eq. (1),

$$|F|^2 = \sum_j |\mu_j| + 2\sum_{i<j} \sqrt{|\mu_i||\mu_j|}\cos\left(2\pi f v \alpha_{ij} t - \Delta\phi_{ij}\right) , \quad (4)$$

where $\boldsymbol{v} = v\,\hat{\boldsymbol{v}}$, $\alpha_{ij} \equiv \hat{\boldsymbol{v}} \cdot (\boldsymbol{\alpha}_i - \boldsymbol{\alpha}_j)$ is the difference in deflection angle between the i-th and j-th image, and $\Delta\phi_{ij} = 2\pi f \Delta t_{ij} - \pi n_{ij}$ is the constant phase shift between the two images, given by the difference of the time delays, $\Delta t_{ij} \equiv t_i - t_j$, and $n_{ij} = (n_i - n_j)$. The first sum consists of single images contribution, while the second arises from their interference. We will define the dimensionless impact parameter as $y = |\boldsymbol{\theta}_s|/\theta_E$, where

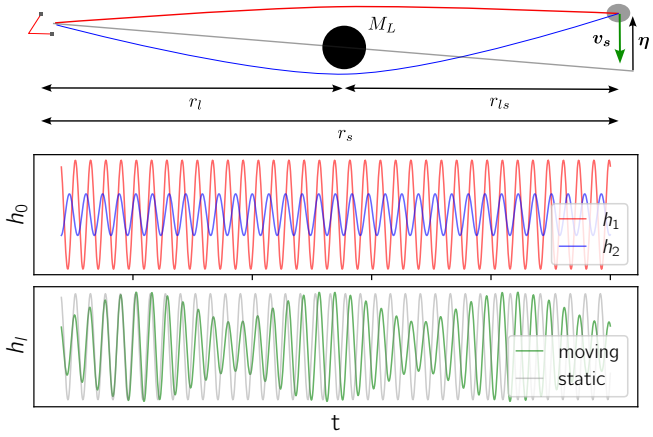

FIG. 1: Strong lensing of a quasi-monochromatic source. Top: Gravitational lensing by Sgr A* forms two images of a rotating pulsar. Here, $\boldsymbol{\eta} = \boldsymbol{\theta}_s r_s$ is the physical impact parameter in the source plane, related to y by $|\boldsymbol{\eta}| = y\theta_E r_s$. Middle: each image is magnified, delayed and slightly red/blue-shifted. Bottom: at the detector, the interference between both images produces an amplitude modulation (here exaggerated for illustrative purposes).

$$\theta_E \equiv \sqrt{\frac{4GM_l r_{ls}}{r_l r_s}} \quad (5)$$

is the Einstein angle. The effect of the relative motion enters, in practice, through the time dependence $y(t) = \sqrt{y_0^2 + \left(\frac{v(t-t_0)}{r_l\theta_E}\right)^2}$, where y_0 is the impact parameter at $t = t_0$.

In the following, we consider that the unlensed wave h_0 is perfectly monochromatic, i.e.,

$$h_0(t, r_s) = \frac{\mathcal{A}}{r_s} e^{-i\phi(t)} , \qquad \phi(t) = 2\pi f_0 t + \phi_0 , \quad (6)$$

where $\mathcal{A}$ depends on the source's orientation and ϕ_0 is the phase value at $t = 0$. From Eq. (1), the lensed waveform in time domain reads

$$h_l(t, r_s, \boldsymbol{\theta}_s) = \frac{\mathcal{A}}{r_s}\sum_j |\mu_j(t)|^{1/2} e^{-i2\pi f_0(t - t_j(t)) - i\pi n_j} , \quad (7)$$

If the effective lens velocity is negligible, the superposition of the images is again a monochromatic signal. In this case, it is impossible to establish if the signal is lensed. However, the lens motion can break this degeneracy thanks to the frequency shift of each image, Eq. (3). Figure 1 shows that the superposition of the two images (middle panel) gives rise to a monochromatic signal for a static lens (grey curve, bottom panel) or a periodic

modulated signal when the lens is moving (green curve, bottom panel).

Given a lensing signal with lens mass M_l, effective lens velocity v and impact parameter y_0, potential information on these parameters is contained in three features: 1) the modulation period,

$$T_{ij} = \frac{1}{f_0 v \alpha_{ij}} = 2.4\,\mathrm{d}\left(\frac{1\mathrm{kHz}}{f_0}\right)\left(\frac{10^{-3}}{v}\right)\left(\frac{1''}{\alpha_{ij}}\right), \quad (8)$$

2) the modulation amplitude $\sqrt{\mu_j/\mu_i}$, which depends purely on $y(t)$ and 3) the modulation phase, given by $\Delta t_{ij} \propto M_l$. To extract information, it is required to observe the modulation over the survey time, $T_{ij} \lesssim T_{\rm obs}$, and measure $\sqrt{\mu_j/\mu_i}$ with sufficient significance.

An additional lensing modulation can arise if the unlensed CW is not perfectly monochromatic, i.e. $\phi(t)/2\pi = f_0(t-t_r) + \frac{\dot f_0}{2}(t-t_r)^2 + \ldots$, with t_r some reference time. This modulation, due to a phase difference between images, appears on a timescale $(\dot f_0 \Delta t_{ij})^{-1} = 317\mathrm{yr}\left(\frac{100\mathrm{s}}{\Delta t_{ij}}\right)\left(\frac{1\mathrm{pHz/s}}{\dot f_0}\right)$. For ms pulsars ($\dot f \lesssim 1$pHz/s) [40] this is much longer than $T_{\rm obs}$ and we will ignore it in our analysis. Note that in CWs, detections are sensitive to $\dot f_0$, as it affects the phase on a timescale $(\dot f_0/2)^{-1/2} = 16.4\,\mathrm{d}\left(\frac{1\mathrm{pHz/s}}{\dot f_0}\right)^{1/2}$. Nevertheless, this effect is common to all images and can be included in the data resampling discussed after Eq. 6 [41].

Other situations that mimic strongly lensed sources can be ruled out. A source in a binary may exhibit an amplitude modulation via precession [42, 43]. However, this can be distinguished from lensing through a periodic phase difference, which is absent for lensed sources moving at constant velocity. The possibility of multiple sources with similar frequency and overlapping sky localization is negligible: to be compatible with lensing, their angular separation must be $\lesssim 10''$ (cf. Fig. 2 below) and their frequencies might differ by no more than $\Delta f/f \lesssim 10^{-7}(\alpha_{ij}/10'')(v/3\times10^{-3})$, see Eq. (3).

Neutron stars lensed by Sgr A*. The framework discussed above can be potentially applied to several astrophysical scenarios. As proof of principle, we focus this letter on studying CWs emitted by isolated spinning neutron stars, lensed by Sgr A*. Hence, we will restrict our analysis to a point lens, which produces two images separated by a time delay $\sim 2GM_l = 39.4\,\mathrm{s}\,(M_l/M_{\mathrm{SgrA}^*})$; see App.A. Figure 2 shows the angular separation of the source and image positions in this case. As the impact parameter typically varies by a small fraction (less than a few %) of Sgr A*'s Einstein radius over the observation period, we can consider the magnification of the images to be approximately constant. However, for lenses with smaller impact parameters or lower masses, the time variation of the impact parameter can cause the modulation amplitude to vary over time, which can further assist in identifying lensed events.

Isolated spinning NSs are expected to produce CWs in the $10^2 - 10^3$ Hz frequency band through a variety of

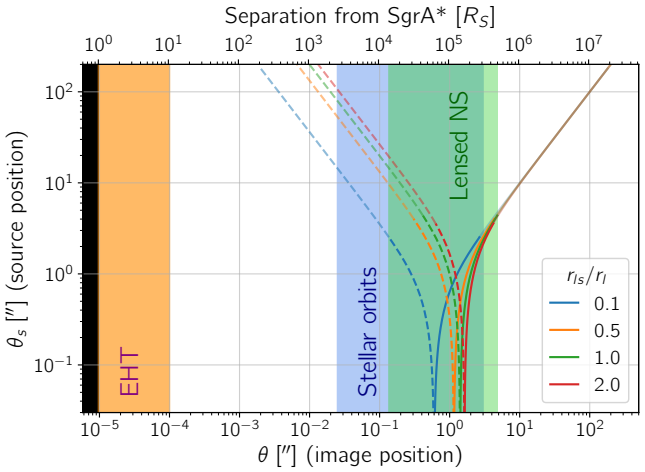

FIG. 2: Source position as a function of the image position (and on the separation measured in Schwarzschild radii R_S), for positive (solid lines) and negative (dashed lines) parity images, for Sgr A* modelled as a point-like lens, for different source distances. Faint lines indicate that no strong evidence of lensing can be established. Shaded areas correspond to the regions that can be probed by different methods.

different mechanisms [26, 27, 44], and could be observed by future ground-based detector campaigns. NSs are expected to have sizeable velocities [45] due to either NS natal kicks ($\sim$ 400 km/s) [46], or the Solar System's motion in the galaxy ($\sim$ 200 km/s) [47–49], necessary to observe the lensing modulation Eq. (8). We will assume that NSs signal can be modelled by a monochromatic waveform, Eq. (6), i.e. the frequency evolution has been included through *demodulating* the signal by transforming the time coordinate $t \to t - t_0 + \dot f_0/(2f_0)(t-t_0)^2 + \cdots$. As explained above, all images of typical NS evolve at the same rate on observable timescales; hence, the demodulation process is common to all.

The waveform (6) also includes a *resampling* to account for the detector's motion $t = t' + \hat n\cdot\vec x(t') + \Delta T$, where t' is the observation time, $\hat n$ is the source's direction, $\vec x$ is the detector's position relative to the Solar System barycenter and ΔT is the relativistic time delay (see Ref. [50], Ch. 7). The antenna pattern (given by $\hat n$) has been factored out of $\mathcal{A}$. As discussed in Ref. [50] (see Eq. 7.151), resampling requires accuracy on the source's position at the level of

$$\delta\theta \lesssim \begin{cases} 22'\left(\frac{T_{\rm coh}}{1\mathrm{d}}\right)^2\left(\frac{\mathrm{kHz}}{f_0}\right) & (1\,\mathrm{d} \lesssim T_{\rm coh} \lesssim 10^2\,\mathrm{d}) \\ 0.065''\left(\frac{1\mathrm{yr}}{T_{\rm coh}}\right)\left(\frac{\mathrm{kHz}}{f_0}\right) & (T_{\rm coh} \gtrsim 10^2\,\mathrm{d}) \end{cases}, \quad (9)$$

where $T_{\rm coh}$ is the coherence time. The limit above corresponds to all-sky NS searches, where a relatively low $T_{\rm coh}$ allows computational efficiency [41]. Since the separation between images is $|\alpha_{12}| \lesssim 10''(M_l/M_{\mathrm{SgrA}^*})$, see Fig. 2, data resampling is common to all images for $T_{\rm coh} \lesssim 1$ week. Once a source is found, follow-up analyses with larger $T_{\rm coh}$ can improve the sky localization, with an

accuracy shown in the second line. This sensitivity is enough to resolve the individual images and even their motion in some cases. Nonetheless, we will not consider this information in our analysis.

The dominant mode of a CW emitted from a NS with non-axisymmetric deformations misaligned with the rotation axis $\hat{z}$ has an amplitude

$$\mathcal{A} = 4\pi^2 G I_{zz} f_0^2 \epsilon \,, \tag{10}$$

where I_{zz} is the moment of inertia of a perpendicular biaxial rotor spinning with axis $\hat{z}$ and the ellipticity parameter, $\epsilon = (I_{xx} - I_{yy})/I_{zz}$, describes the degree of deviation from spherical symmetry around the rotation axis of the star. Here we assume the fiducial value $I_{zz} = 10^{38}\,\mathrm{kg\,m^2}$ [23].

The lack of detection of CWs in the first three observational campaigns of the ground-based LVK detector network has produced frequency-dependent upper limits on their amplitude [23, 24, 51]. Upper limits on $\mathcal{A}$ can be translated into bounds on ϵ at a fixed distance. For instance, according to the most up-to-date bounds [23, 51], searches would be sensitive to CWs emitted from NSs at 550 Hz with $\epsilon > 5 \cdot 10^{-7}$ within 1 kpc distance and $\epsilon > 2 \cdot 10^{-6}$ within 10 kpc distance at 1550 Hz. We will adopt a compatible fiducial value $\epsilon = 10^{-7}$ in our analysis. This value is also consistent with theoretical expectations [52, 53], while population-based studies suggest a lower bound, $\epsilon \gtrsim 10^{-9}$ [40]. Next-generation GW detectors will be capable of observing NSs up to distances of [50]

$$r_{\rm hor} = 35\,\mathrm{kpc} \times \left(\frac{\epsilon}{10^{-7}}\right) \left(\frac{f_0}{800\,\mathrm{Hz}}\right)^2 \left(\frac{T_{\rm obs}}{10\,\mathrm{yr}}\right)^{1/2} \gamma \,, \tag{11}$$

where we have defined an efficiency factor, $\gamma \equiv \left(\frac{3750}{\mathcal{N}}\right)^{1/4} \left(\frac{4}{\mathrm{SNR_{thr}}}\right) \left(\frac{4.8\,10^{-25}}{\sqrt{S_n(f_0)\,\mathrm{Hz}}}\right)$. Here, $\mathrm{SNR_{thr}}$ is the signal-to-noise ratio (SNR) threshold of the search and $\mathcal{N} = T_{\rm obs}/T_{\rm coh}$ is the number of stacks in which the data is divided.

A fraction of NSs in our galaxy, depending on the actual spatial distribution of the population, are expected to lie close to the line of sight to Sgr A*. The probability of this occurrence was addressed in Ref. [37], by considering various spatial distribution models for galactic NSs capturing uncertainties in formation proprieties, such as different natal velocities and evolution history in the galactic potential. Assuming an ellipticity of $\epsilon = 10^{-7}$ for the population, the authors find that the probability of detecting one or more lensed events is $1 - 36\%$ for LVK O5 and $2 - 55\%$ for 3G detectors. Their statistical study assumes that lensing is observed if sources lie within the Einstein radius. However, as we will show below, 3G detectors can test the lensing hypothesis at angular separations several times larger than the Einstein angle, increasing the prospects of detection. We address the impact of this extension in App. B.

Lens parameter estimation. To study the prospect of measuring the lens mass, the impact parameter and the effective lens velocity we run a numerical Monte Carlo (MC) simulation to compute the marginalized posteriors of these parameters. We assume a 3G detector network consisting of a single Einstein Telescope and an in-band signal duration $T_{\rm obs} = 10\,\mathrm{yr}$. As a fiducial setup, we consider a point-like lens with mass $M_l = 4.154 \cdot 10^6\,M_\odot$ (i.e. the measured mass of Sgr A* [54]) and effective lens velocity $v = 10^{-3}$, at a distance $r_l = 8.5\,\mathrm{kpc}$. The source is a spinning NS with ellipticity $\epsilon = 10^{-7}$, emitting CWs at a frequency $f_0 = 800\,\mathrm{Hz}$ and relative distance $r_{ls} = r_l$. We will also discuss how the results change when straying from these fiducial values. The parameter inference and details about the sampling are discussed in Apps. C and D.

Figure 3 shows 1-d, 68% C.L. limits on the lensing parameters from the 1-d marginalized posteriors, obtained from the MC simulation as a function of the initial impact parameter y_0 (fiducial setup). Since the mass of Sgr A* is known with sub-percent accuracy [54] and is expected to be more constrained in the future, we run two analyses: with M_l as a free parameter and fixed to the known value. In both cases, the lens parameters can be extracted from the signal beyond $y_0 = 1$. For example, for $y_0 = 3$ all parameters are constrained with a relative error smaller than 50% at 1σ C.L. At large enough y_0, the sampled contours become consistent with $\mu_2 = 0$ (no second image detected) and lens parameters cannot be constrained (see Fig. 9 in App. D). Note that, for strictly monochromatic sources, M_l and v can be constrained only up to a periodic factor, as they only enter the GW signal phase, see Eq. (7).

Figure 4 shows the 1- and 2-d 95% C.L. marginalized lens parameter posteriors from the MC (the complete set of posteriors is shown in App. D). At large impact parameters, the posteriors stray from the Gaussian limit. The lack of gaussianity becomes apparent for the $y_0 = 3$ contour.

To assess our capacity to distinguish the lensed from the null—unlensed—hypothesis, we carry out statistical hypothesis testing. Figure 5 shows the Bayes ratio between the moving lens model and the unlensed model, $\mathcal{B}_{LU}$, as a function of the initial impact parameter, for different distance ratios r_{ls}/r_l. For impact parameter $y_0 < 3$, the lensing hypothesis can be assessed with at least *strong evidence* ($\log \mathcal{B}_{LU} > 10$, cf. I in App. C), extending to larger impact parameters depending on r_{ls}. Fixing the lens mass improves the results only for small y_0, as for parameter inference (see above). For lower effective lens velocities, $v = 10^{-5}$, the Bayes ratio curve closely overlaps with the fiducial case, with the value at $y_0 = 3$ being only slightly smaller but still above the strong-evidence threshold. Note that the evidence for the unlensed and static lens hypotheses are identical, as they are both degenerate for a monochromatic signal.

We explored different lensing configurations varying the fiducial parameters. In the limit of large SNR, the co-

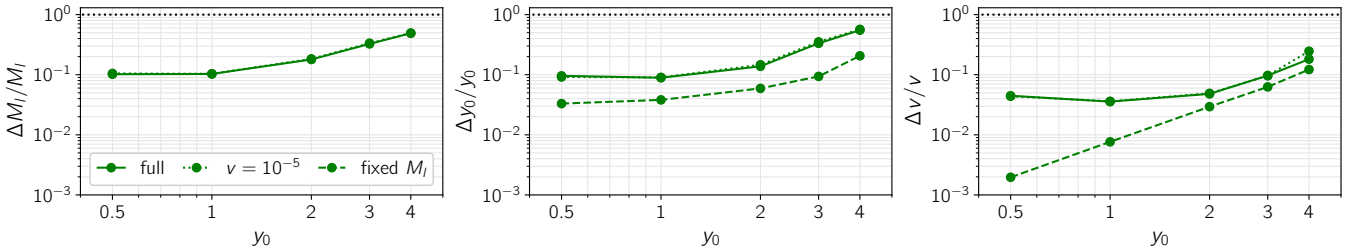

FIG. 3: 68% C.L. relative bounds on inferred lens parameters from MC simulations plotted against the initial dimensionless impact parameter, for the fiducial setup described in the text. Two cases are considered: uniform prior on the lens mass (solid line); fixed lens mass (dashed line). For uniform prior, the inferred bounds are unchanged when considering a smaller relative velocity, $v = 10^{-5}$ (overlapping dotted line).

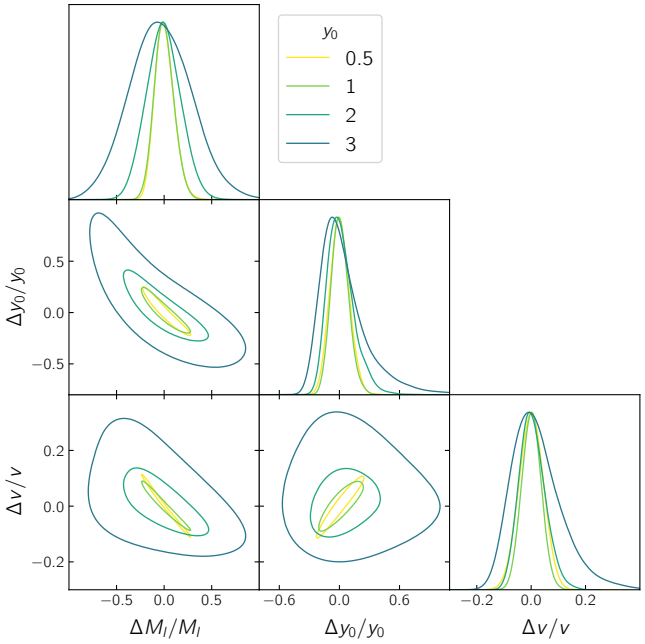

FIG. 4: 1-d and 2-d marginalized 2-σ C.L. posteriors of the lens parameters, for different initial impact parameters, for the fiducial setup discussed in the text.

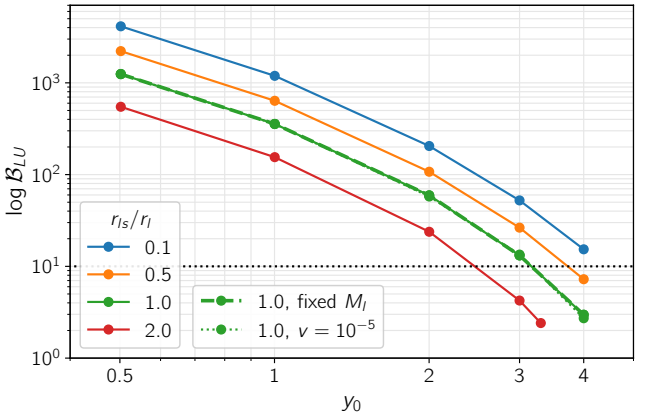

FIG. 5: Bayes' ratio of lensed vs unlensed hypothesis plotted against the initial impact parameter for multiple distance ratios, r_{ls}/r_l, for the fiducial setup. For $\log \mathcal{B}_{LU} > 10$ (dotted black line), the lensing hypothesis has *strong evidence*. The dashed and dotted green lines that overlap with the solid green line show the fixed M_l and $v = 10^{-5}$ case, respectively.

variance matrix scales as the inverse of the SNR. Thus, we can read from Eq. (C6) how the expected accuracy scales with the signal amplitude and observation time. For fixed SNR, changing the frequency of the source influences our results only marginally. This is true as long as the modulation period in Eq. (8) is smaller or comparable to the observation time. For the same reason, varying the effective lens velocity within the range $10^{-2} - 10^{-5}$ has a very small impact on our results. The parameter that has the major impact is the source-lens distance ratio, r_{ls}/r_s, with smaller values leading to more accurate parameter estimation.

Discussion and prospects. We have analyzed the phenomenology of strongly-lensed, quasi-monochromatic GW signals. A relative transverse velocity causes an amplitude modulation of the waveform, see Figs. 1 and 6, that can be used to constrain the lens parameters. Using Bayesian methods and specializing in the geometric optics regime, we have established the capacity of GW detectors to recover lens and source parameters depending on the lens configuration. We have focused on monochromatic isolated neutron stars lensed by Sgr A*, the massive black hole at the MW's centre, as observed by the Einstein Telescope. Parameter estimation is expected to improve using data from multiple 3G detectors in a global network [21], thanks to the increased SNR and sky coverage.

The parameters of the lens, (M_l, y_0, v), and the source, $(\mathcal{A}/r_s, f_0, \phi_0)$, can be accurately measured even for large impact parameter y_0, despite degenerate posteriors; see Figs. 3 and 4. Precise parameter inference and strong evidence for the lensed signal (log Bayes' ratio ≥ 10) can be robustly established for $y_0 < y_{\rm max} \approx 5 - 3$ for $r_{ls}/r_l = 0.1 - 1.5$; Fig. 5. In contrast, advanced LIGO requires a closer alignment ($y_{\rm max} \simeq 1.5$ for $r_{ls}/r_l = 1$). The results depend mildly on the source's frequency, mainly through the SNR via the detector's noise curve. Fixing

Sgr A*'s mass to its known value increases the precision on the other lens parameters, especially on v at low y_0, as shown in Figs. 3 and 5. While parameter estimation requires a non-zero v, the error is rather insensitive to its exact value as long as $v \gtrsim 10^{-5} \approx 3\,\mathrm{km/s}$, which is high enough to observe the modulation period, see Eq. (8). Thus, small velocities are not an impediment to observing lensed NS. Moreover, the sensitivity to very small velocities suggests that CWs could measure lens accelerations accurately.

An immediate consequence of these results is an optimistic revision of the detection probabilities. Reference [37] considered the number of sources within the Einstein angle of Sgr A*, $y_{\max} \leq 1$. Because lensing probabilities scale as $\propto y_{\max}^2$, being able to identify lens sources at larger impact parameters improves the detection prospects substantially: assuming detectability below the strong-evidence threshold, as motivated by Fig. 5, increases the expected number of sources by one order of magnitude. A simple model for the NS distribution [36] gives an average of $3.36\,(0.1\,\mathrm{kpc}/\Delta z)(N_0/10^8)$ detections, where N_0 is the number of observable NSs and Δz is their spread perpendicular to the galactic plane (see App. B for details). While the ultimate prospects depend on unknown astrophysics, a targeted search of NSs lensed by Sgr A* by 3G detectors is warranted.

Such a detection would provide a unique probe of the galactic center. Detection of lensed EM radiation from objects closely aligned with Sgr A* is challenging due to abundant stars, gas and dust in the central region of the galaxy [55]. In contrast, lensed CWs are negligibly absorbed and may provide a pristine view of the region near our supermassive black hole. CW detection can achieve precise angular localization, facilitating source localization by EM observations. As the secondary image forms close to the lens, $x_2 \sim 1/y_0$, sources at sizeable angular separation would prove particularly useful to probe the vicinity of the central black hole. Since lensing is sensitive to the enclosed mass up to the image location, CWs can probe the vicinity of Sgr A* in the range $10^4 - 10^5 R_S$ complementary to BH imaging ($\sim 1 - 10\,R_S$ [56]) and stellar orbits ($\sim 10^3 - 10^5\,R_S$) [57], see Fig. 2.

Comparing M_l to the mass of Sgr A*, measured by other means, constrains the matter distribution in the galactic center, and could serve to find or rule out dark matter spikes [58] or cores formed by ultra-light scalars [59]. Subdominant effects, such as microlensing, could serve to further constrain compact objects and substructures in the vicinity of Sgr A*. CWs lensed by Sgr A* would also provide very precise tests of GW propagation in extreme environments [60, 61].

This study is the first step towards understanding parameter reconstruction in lensed CWs. Our analysis has relied exclusively on the modulation due to interference between multiple images. However, the precise sky localization achievable by follow-up analyses (Eq. 9) can provide additional information (i.e. through image positions and perhaps even their motion), substantially boosting the precision found in our analysis. Including time dependence of the magnifications, next-order variation of the time delay and wave-optics corrections will allow us to address light lenses and to study microlensing around Sgr A*. Further extending our framework beyond the point-like lens may enable CWs to probe lenses other than our supermassive black hole. This will enable novel probes of galactic substructure and fundamental physics, even if NS observable by 3G detectors are not abundant enough for CWs lensed by Sgr A* to be observed.

Acknowledgments

We are very grateful to Soummyadip Basak and Giovanni Tambalo for discussions, as well as Lorenzo Speri, Jonathan Gair and Ollie Burke for help with aspects of the parameter estimation.

Appendix A: Gravitational lensing with a moving lens

To compute the amplification factor due to the presence of a lens, we follow the standard derivations [4, 38] for a lens at rest. Indeed, one can always perform a Lorentz boost to the lens frame, where the line element of the metric is static and reads

$$ds^2 = -(1+2U)\,dt^2 + (1-2U)\,d\vec{r}^{\,2}\,, \tag{A1}$$

where $U(\vec{r})$ is the gravitational potential generated by the lens. With this metric, the wave equation $\partial_\mu(\sqrt{-g}g^{\mu\nu}\partial_\nu h) = 0$ becomes, at linear order in U,

$$\left(\nabla^2 + \omega^2\right)\tilde{h}(\omega,\vec{r}) = 4\omega^2 U(\vec{r})\tilde{h}(\omega,\vec{r})\,. \tag{A2}$$

We want to compute the amplification factor $F \equiv \tilde{h}/\tilde{h}_0$. It is useful first to define the quantities intervening in the final result. Using spherical coordinates centred at the observer, $\vec{r} = (r,\theta,\varphi)$, and working for small angles, $\theta \ll 1$, we first define the two-dimensional vector $\boldsymbol{\theta} = \theta(\cos\varphi, \sin\varphi)$ and denote by $\boldsymbol{\theta}_l$ and $\boldsymbol{\theta}_s$ the observed and true angular position of the source, respectively.

For a thin lens, F can be computed from the above wave equation, Eq. (A2), and it is given in the form of a diffraction integral [38],

$$F(\omega,\boldsymbol{\theta}_s) = \frac{\omega}{2\pi i}\frac{r_l r_s}{r_{ls}}\int d^2\boldsymbol{\theta}\,\exp[i\omega t(\boldsymbol{\theta},\boldsymbol{\theta}_s)]\,, \tag{A3}$$

where

$$t(\boldsymbol{\theta},\boldsymbol{\theta}_s) = \frac{r_l r_s}{2r_{ls}}|\boldsymbol{\theta}-\boldsymbol{\theta}_s|^2 - \hat{\psi}(\boldsymbol{\theta})\,, \tag{A4}$$

given the lensing potential $\hat{\psi}(\boldsymbol{\theta}) \equiv \int dr\,U(r,\boldsymbol{\theta})$. It is also convenient to introduce the so-called Fermat potential, $T(\boldsymbol{\theta},\boldsymbol{\theta}_s) = t(\boldsymbol{\theta},\boldsymbol{\theta}_s)/(4GM_l)$, the dimensionless frequency, $w \equiv 4GM_l\,\omega$, and the dimensionless impact parameter,

$y = |\boldsymbol{\theta}_s|/\theta_E$. Figure 6 shows $|F|$ as a function of w and y. The geometric optics limit applies for $wT(\boldsymbol{\theta}, \boldsymbol{\theta}_s) \gg 1$. In this case, the diffraction integral is dominated by the stationary points of the Fermat potential,

$$\nabla_{\boldsymbol{\theta}} T = 0 \,, \tag{A5}$$

which is the lens equation [62], and reduces to a discrete sum over multiple images, as in Eq. (1).

For instance, a point-like lens always splits the source in two images, characterized by the following magnifications and time delay, respectively [62],

$$\frac{\mu_2}{\mu_1} = \frac{2 - y(\sqrt{y^2+4} - y)}{2 + y(\sqrt{y^2+4} + y)} \,,$$
$$\Delta t_{12} = 2GM_l \left[y\sqrt{y^2+4} + 2\log\left(\frac{\sqrt{y^2+4}+y}{\sqrt{y^2+4}-y} \right) \right] \,,$$

where the separation between the two images and the difference in deflection angle are, respectively, $\Delta x_{12} \equiv |\boldsymbol{\theta}_{l,1} - \boldsymbol{\theta}_{l,2}|/\theta_E = \sqrt{y^2+4}$ and $\Delta\alpha_{12} = 5.8'' \, \Delta x_{12} \left(\frac{r_s \, 8.5\,\mathrm{kpc}}{2 r_{ls} r_l} \frac{M_l}{M_{\mathrm{SgrA}^*}} \right)^{1/2}$.

In the lens frame, a moving observer or a moving source induce a time dependence in the source position $\boldsymbol{\theta}_s$, as discussed in the text. If the frequency of the wave is much smaller than the typical rate of change of the Fermat potential, $\dot{T}/T$, which is never the case for the above study, the previous derivation needs to be corrected by non-linear terms: the right-hand side of Eq. (A2) is modified into $4\omega^2 \left(1 - \frac{2}{\omega} \vec{v} \cdot \nabla\right) \int d\omega' \, \tilde{U}(\omega' - \omega, \vec{r}) \, \tilde{h}(\omega', \vec{r})$, which couples different frequencies.

Another effect appears when we want to relate the time delay in the lens frame to the one in the source frame by a Lorentz boost. This affects the time delay only if the velocity of the lens is along the undeflected trajectory. Since the boost affects the undeflected and deflected trajectories in the same way, it has no effect on the geometrical time delay. The Shapiro time delay instead receives a Doppler correction [63, 64], $\Delta t_{\mathrm{Shapiro}} = (1 - \vec{v}_l \cdot \hat{n}) \hat{\psi}$, where $\hat{\psi}$ is the lensing potential for a lens at rest. We do not consider this effect, which is common to all images and hence not measurable.

Appendix B: Lensing probability

We will now estimate the probability of strong lensing and compare it with previous results. We will follow the source distribution proposed in Ref. [36] (also considered in Ref. [37])

$$\frac{dP_s(r,z)}{dV} = \frac{1}{2\pi} \frac{1}{\sigma_r^2} e^{-\frac{r^2}{2\sigma_r^2}} \frac{1}{2\Delta z} e^{-\frac{|z|}{\Delta z}} \,. \tag{B1}$$

Here $dV = dr r d\phi dz$ is the volume element, $\sigma_r = 5$kpc is the scatter of sources in the galactic plane and Δz is perpendicular to it. We will assume that the Earth and any detectable lensed source deviate negligible from the galactic plane, relative to $\Delta z \sim 0.1 - 1$kpc, and set $z \approx 0$.

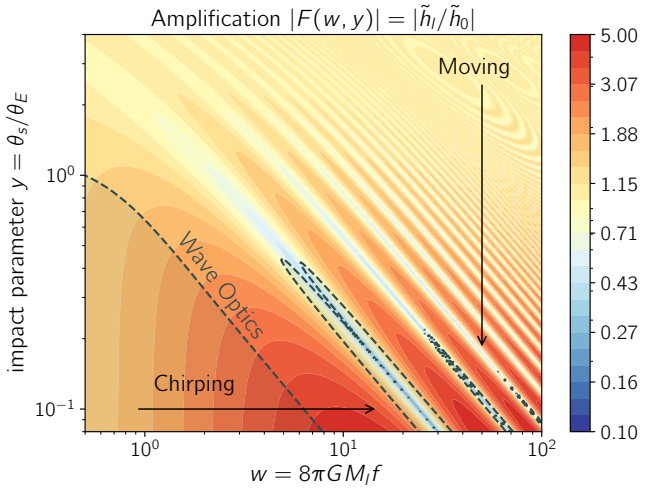

FIG. 6: Amplification factor as a function of the dimensionless frequency $w = 8\pi G M_l \, f$ and impact parameter $y = |\boldsymbol{\theta}_s|/\theta_E$. The full-wave solution is shown for a point-like lens. Dashed gray contours correspond to the transition between wave and geometric optics regimes (less than 10% relative difference). Our fiducial system lies in geometric optics with $w = 8\pi G M_{\mathrm{SgrA}^*} f_0 \simeq 10^3 - 10^4$. Diffraction and wave effects can be observed for chirping binaries (varying w and keeping y constant) or moving lens systems (varying y and keeping w constant).

The fraction of strongly lensed sources is

$$f_l \equiv \frac{\bar{N}_l}{N_0} \approx \int_0^{r_{\mathrm{hor}}} dr_{ls} r_{ls} (r_l + r_{ls}) \left(\theta_E y_{\mathrm{max}}\right)^2 \frac{dP_s}{dV} \,, \tag{B2}$$

were $\bar{N}_l$ is the average number of lensed sources and N_0 is the number of observable sources [37]. The integral is performed up to a detection horizon r_{hor} (cf. Eq. 11) and y_{max} is the highest value of the impact parameter for which very strong evidence for lensing can be established, see Fig. 5. For $r_{ls}/r_l \geq 0.5$, y_{max} obeys a linear relation, which we have extrapolated to the whole domain to compute the integral above. This underestimates y_{max} close to the lens (stars vs line in Fig. 7) and is thus a conservative assumption.

Figure 7 shows the fraction of lensed NSs with strong evidence, $f_l[y_{\mathrm{max}}]$, as a function of r_{hor}, where we also show the fraction of sources within the Einstein radius, $f_l[y = 1]$, obtained from setting $y_{\mathrm{max}} \to 1$ in Eq. (B2). The Einstein radius, source distribution and strong-evidence parameter entering the calculation are also shown. For $r_{\mathrm{hor}} \gtrsim 1.5\, r_l$, the expected number of observed sources is

$$\bar{N}_L = 3.36 \left(\frac{0.1\mathrm{kpc}}{\Delta z} \right) \left(\frac{N_0}{10^8} \right) \,. \tag{B3}$$

This is a factor ~ 9.04 larger than the estimate obtained setting $y_{\mathrm{max}} = 1$ in Eq. (B2), as in the analysis

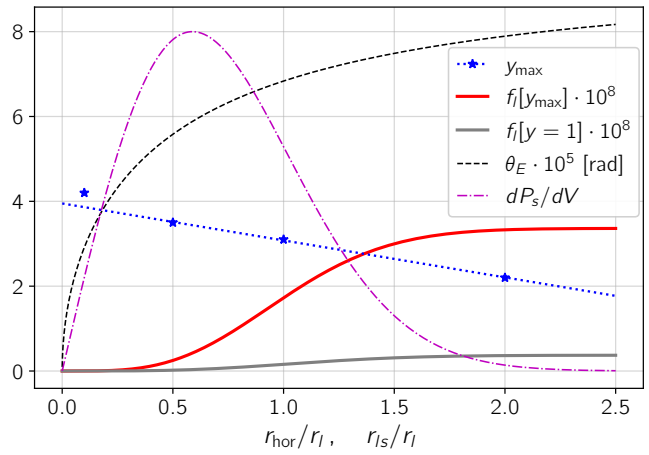

FIG. 7: Expected fraction of NSs lensed by Sgr A* using the strong-evidence cutoff (thick solid red) and the Einstein radius cutoff (thick solid gray), both for $\Delta z = 0.1$kpc. Thin lines represent other quantities appearing in Eq. (B2), stars denote the values of $y_{\rm max}$ obtained from MC sampling, the dotted line is the interpolation used.

of Ref. [37]. The number of detected sources is given by Poisson statistics, with

$$P_l(k) = \frac{\bar{N}_l^k}{k!} e^{-\bar{N}_l}\,, \tag{B4}$$

where k is the number of detections. Hence, the probability of detecting at least a single lensed event is $P_l(k \geq 1) = 1 - e^{-N_l}$. The analysis in Ref. [37] uses $N_0 = 10^9$ as a fiducial number of observable sources. In that case, our study would suggest that more than 34 strong-evidence lensed events could be observed, with $\sim 2\cdot 10^{-15}$ chance of observing none.

Appendix C: Parameter inference

The signal observed at the detector, $d(t)$, is a superposition between background noise and the true gravitational waves signal,

$$d(t) = h(t;\boldsymbol{\theta}) + n(t). \tag{C1}$$

The probability of observing some data d with an incoming gravitational wave signal $h(\boldsymbol{\theta})$ is equivalent to the probability of observing a particular realisation of the noise n. The vector $\boldsymbol{\theta}$ includes the parameters that determine the propagated waveform. For a stationary and Gaussian distributed noise, a realisation n_0 has a probability

$$p(n_0) \propto \exp\left[-\frac{1}{2}\int df \frac{|\tilde{n}_o(f)|^2}{S_n(f)}\right]\,, \tag{C2}$$

where the one-sided power spectral density of noise, $S_n(f)$, is the variance associated with the noise distribution.

The probability of observing d given $\boldsymbol{\theta}$, i.e. the *likelihood* of the parameters $\boldsymbol{\theta}$, is

$$\log p(d \mid \boldsymbol{\theta}) \propto -\frac{1}{2}(d - h(\boldsymbol{\theta}), d - h(\boldsymbol{\theta}))\,, \tag{C3}$$

where the inner product for two signals f and g, in the Fourier space, is defined as

$$(f,g) = 4\,\mathrm{Re}\left[\int_0^\infty df\, \frac{\tilde{h}^\star(f)\,\tilde{g}(f)}{S_n(f)}\right]\,. \tag{C4}$$

For quasi-monochromatic sources, the inner product in Eq. (C4) can be equivalently defined in the time-domain, following Ref. [65, 66], as

$$(h,g) = \frac{2}{S_n(f_0)}\int_0^{T_{obs}} h(t)g(t)\,, \tag{C5}$$

with T_{obs} the observational time. Hence, the SNR, which measures the loudness of the signal, reads

$$\rho \equiv (h|h) \simeq \sqrt{\frac{\mathcal{A}^2}{r_s^2}\frac{T_{\rm obs}}{S_n(f_0)}}\,. \tag{C6}$$

The posterior of $\boldsymbol{\theta}$ is obtained from the likelihood using Bayes' rule, i.e.,

$$p(\boldsymbol{\theta} \mid d) = \frac{p(d \mid \boldsymbol{\theta})p(\boldsymbol{\theta})}{p(d|\mathcal{M}_i)}\,, \tag{C7}$$

where $p(\boldsymbol{\theta})$ is the parameter prior and $p(d|\mathcal{M}_i)$, namely the *evidence*, is the marginal likelihood for a given model $\mathcal{M}_i$:

$$p(d|\mathcal{M}_i) = \int d\boldsymbol{\theta} p(d|\boldsymbol{\theta})p(\boldsymbol{\theta})\,. \tag{C8}$$

In the Bayesian context, the marginalized posteriors are the probability distribution functions of the parameters.

Given two models $\mathcal{M}_i$ and $\mathcal{M}_j$, the ratio of their evidences, called the *Bayes factor*, is used as an index to test different interpretations of the same data:

$$\mathcal{B}_{ij} = \frac{p(d|\mathcal{M}_i)}{p(d|\mathcal{M}_j)}\,. \tag{C9}$$

Following the empirical Jeffrey's prescription [67], in Tab. I we report the range of value of $\mathcal{B}_{ij}$ and the corresponding degree of evidence of the model $\mathcal{M}_i$ over $\mathcal{M}_j$.

Appendix D: Sampling methods

Combining the lensed waveform in Eq. (7) with Eq. (C5) we get the analytical likelihood function for CWs events lensed by SgrA*. We use the dynamic nested sampling package Dynesty [68] to infer parameter posteriors and the evidence of fitting models through numerical MC simulations.

$\log \mathcal{B}_{10}$	$\mathcal{B}_{10}$	Evidence against H_0
2 to 6	3 to 20	Positive
6 to 10	20 to 150	Strong
>10	>150	Very Strong

TABLE I: Evidence against the null hypothesis compared to ranges of Bayes factor.

Our analysis is restricted to the source and lens parameters that are potentially correlated. In particular, the source is assumed to be purely monochromatic and modelled by $(\mathcal{A}/r_s, f_0, \phi_0)$. The lens is modelled initially by :

$$u = \sqrt{\frac{\mu_2}{\mu_1}}, \quad k = \Delta\phi_{21}, \quad z = \frac{\Delta f_{21}}{f}\,, \tag{D1}$$

where $\Delta\phi_{21}$ is the constant phase difference between the two images and Δf_{21} is the relative frequency shift induced by lens motion. The numerical samples are then converted to the point-lens parameters $\{M_l, y_0, v\}$.

In Fig. 8, we present the complete set of 1-d and 2-d marginalized 2-σ posteriors for the fiducial setup, already partially presented in Fig. 4. Figure 9 shows the posteriors of the corresponding original sampling parameters $\{u, k, z\}$. For impact parameter $y \gtrsim 4$, the lack of resolution of the small amplitude modulation, i.e. the r contour being compatible with $r = 0$, prevents the reconstruction of the lensing parameters.

[1] M. Bartelmann, Class. Quant. Grav. **27**, 233001 (2010), 1010.3829.
[2] M. Oguri, Rept. Prog. Phys. **82**, 126901 (2019), 1907.06830.
[3] K. Liao, M. Biesiada, and Z.-H. Zhu, Chin. Phys. Lett. **39**, 119801 (2022), 2207.13489.
[4] R. Takahashi and T. Nakamura, Astrophys. J. **595**, 1039 (2003), astro-ph/0305055.
[5] L. Dai, S.-S. Li, B. Zackay, S. Mao, and Y. Lu, Phys. Rev. D **98**, 104029 (2018), 1810.00003.
[6] M. Çalışkan, L. Ji, R. Cotesta, E. Berti, M. Kamionkowski, and S. Marsat (2022), 2206.02803.
[7] G. Tambalo, M. Zumalacárregui, L. Dai, and M. H.-Y. Cheung (2022), 2210.05658.
[8] G. Tambalo, M. Zumalacárregui, L. Dai, and M. H.-Y. Cheung (2022), 2212.11960.
[9] L. Dai and T. Venumadhav (2017), 1702.04724.
[10] J. M. Ezquiaga, D. E. Holz, W. Hu, M. Lagos, and R. M. Wald, Phys. Rev. D **103**, 064047 (2021), 2008.12814.
[11] A. Vijaykumar, A. K. Mehta, and A. Ganguly (2022), 2202.06334.
[12] O. A. Hannuksela, K. Haris, K. K. Y. Ng, S. Kumar, A. K. Mehta, D. Keitel, T. G. F. Li, and P. Ajith, Astrophys. J. Lett. **874**, L2 (2019), 1901.02674.
[13] L. Dai, B. Zackay, T. Venumadhav, J. Roulet, and M. Zaldarriaga (2020), 2007.12709.
[14] R. Abbott et al. (LIGO Scientific, VIRGO), Astrophys. J. **923**, 14 (2021), 2105.06384.
[15] S. Basak, A. Ganguly, K. Haris, S. Kapadia, A. K. Mehta, and P. Ajith, Astrophys. J. Lett. **926**, L28 (2022), 2109.06456.
[16] K. K. Y. Ng, K. W. K. Wong, T. Broadhurst, and T. G. F. Li, Phys. Rev. D **97**, 023012 (2018), 1703.06319.
[17] F. Xu, J. M. Ezquiaga, and D. E. Holz, Astrophys. J. **929**, 9 (2022), 2105.14390.
[18] P. Amaro-Seoane et al. (LISA) (2017), 1702.00786.
[19] A. Sesana, Phys. Rev. Lett. **116**, 231102 (2016), 1602.06951.
[20] T. Wagg, F. S. Broekgaarden, S. E. de Mink, L. A. C. van Son, N. Frankel, and S. Justham, Astrophys. J. **937**, 118 (2022), 2111.13704.
[21] V. Kalogera et al. (2021), 2111.06990.
[22] A. L. Miller, S. Clesse, F. De Lillo, G. Bruno, A. Depasse, and A. Tanasijczuk, Phys. Dark Univ. **32**, 100836 (2021), 2012.12983.
[23] R. Abbott et al. (LIGO Scientific, VIRGO, KAGRA) (2022), 2201.00697.
[24] V. Dergachev and M. A. Papa (2022), 2202.10598.
[25] K. Riles, Mod. Phys. Lett. A **32**, 1730035 (2017), 1712.05897.
[26] M. Sieniawska and M. Bejger, Universe **5**, 217 (2019), URL `https://doi.org/10.3390%2Funiverse5110217`.
[27] P. O. Juliana, *Status and perspectives of continuous gravitational wave searches* (2022), URL `https://arxiv.org/abs/2202.01088`.
[28] K. Riles (2022), 2206.06447.
[29] K. Liao, M. Biesiada, and X.-L. Fan, Astrophys. J. **875**, 139 (2019), 1903.06612.
[30] A. G. Suvorov, Astrophys. J. **930**, 13 (2022), 2112.01670.
[31] T. Naderi, A. Mehrabi, and S. Rahvar, Phys. Rev. D **97**, 103507 (2018), 1711.06312.
[32] A. Katz, J. Kopp, S. Sibiryakov, and W. Xue, JCAP **12**, 005 (2018), 1807.11495.
[33] A. Katz, J. Kopp, S. Sibiryakov, and W. Xue, Mon. Not. Roy. Astron. Soc. **496**, 564 (2020), 1912.07620.
[34] D. L. Jow, S. Foreman, U.-L. Pen, and W. Zhu, Monthly Notices of the Royal Astronomical Society **497**, 4956 (2020), ISSN 1365-2966, URL `http://dx.doi.org/10.1093/mnras/staa2230`.
[35] R. Narayan, Astrophys. J. **319**, 162 (1987).
[36] B. T. Reed, A. Deibel, and C. J. Horowitz, Astrophys. J. **921**, 89 (2021), 2104.00771.
[37] S. Basak, A. K. Sharma, S. J. Kapadia, and P. Ajith (2022), 2205.00022.
[38] T. T. Nakamura and S. Deguchi, Progress of Theoretical Physics Supplement **133**, 137 (1999), ISSN 0375-9687, https://academic.oup.com/ptps/article-pdf/doi/10.1143/PTPS.133.137/5283012/133-137.pdf, URL `https://doi.org/10.1143/PTPS.133.137`.
[39] R. Kayser, S. Refsdal, and R. Stabell, Symposium - In-

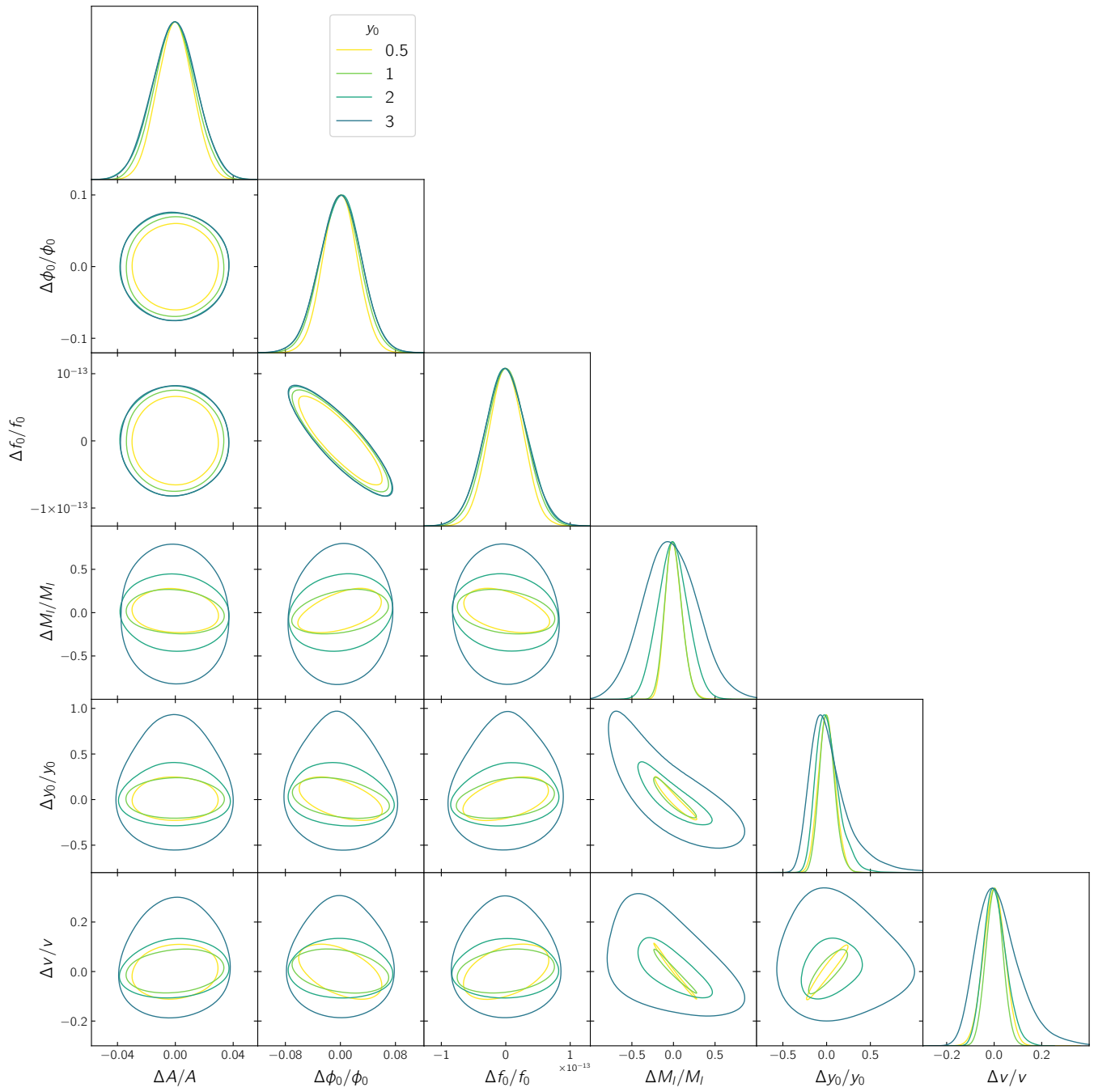

FIG. 8: 1-d and 2-d marginalized 2-σ posteriors of the full set of source and lens parameters, for the fiducial setup discussed in the text. Here, $A \equiv \mathcal{A}/r_s$.

ternational Astronomical Union **166**, 36 (1986).

[40] G. Woan, M. D. Pitkin, B. Haskell, D. I. Jones, and P. D. Lasky, Astrophys. J. Lett. **863**, L40 (2018), 1806.02822.

[41] P. R. Brady, T. Creighton, C. Cutler, and B. F. Schutz, Phys. Rev. D **57**, 2101 (1998), gr-qc/9702050.

[42] T. A. Apostolatos, C. Cutler, G. J. Sussman, and K. S. Thorne, Phys. Rev. D **49**, 6274 (1994).

[43] R. P. Breton, V. M. Kaspi, M. Kramer, M. A. McLaughlin, M. Lyutikov, S. M. Ransom, I. H. Stairs, R. D. Ferdman, F. Camilo, and A. Possenti, Science **321**, 104 (2008), 0807.2644.

[44] K. Glampedakis and L. Gualtieri, in *The Physics and Astrophysics of Neutron Stars* (Springer International Publishing, 2018), pp. 673–736, URL `https://doi.org/10.1007%2F978-3-319-97616-7_12`.

[45] N. Sartore, E. Ripamonti, A. Treves, and R. Turolla, Astron. Astrophys. **510**, A23 (2010), 0908.3182.

[46] G. Hobbs, D. R. Lorimer, A. G. Lyne, and M. Kramer, Mon. Not. Roy. Astron. Soc. **360**, 974 (2005), astro-ph/0504584.

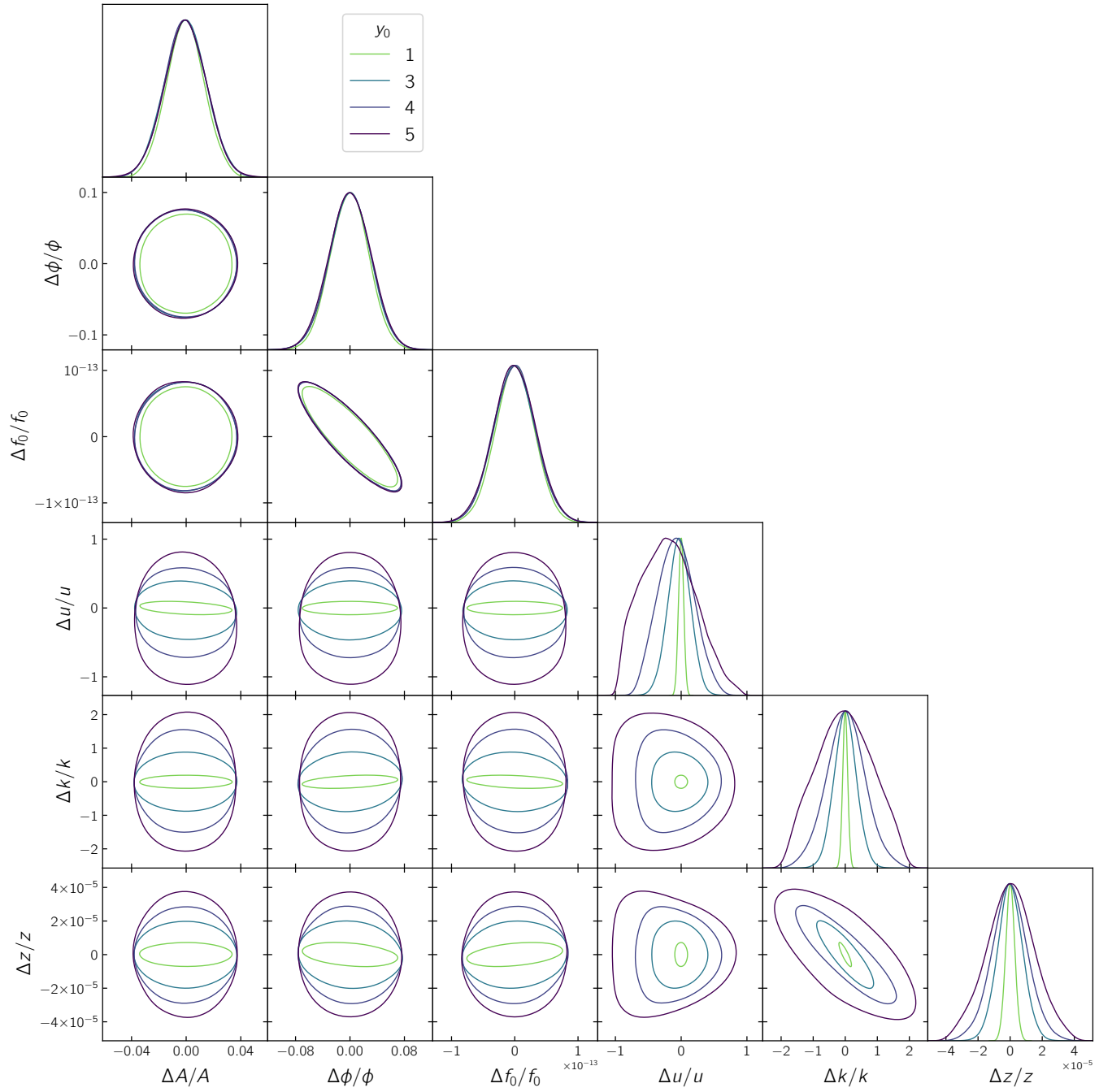

FIG. 9: 1-d and 2-d marginalized 2-σ posteriors of the full set of source and lens parameters, with the letter expressed in terms of the original sampling parameters, for the fiducial setup discussed in the text. Here, $A \equiv \mathcal{A}/r_s$.

[47] Y. Sofue, M. Honma, and T. Omodaka, Publ. Astron. Soc. Jap. **61**, 227 (2009), 0811.0859.

[48] P. Mró z, A. Udalski, D. M. Skowron, J. Skowron, I. Soszyński, P. Pietrukowicz, M. K. Szymański, R. Poleski, S. Kozłowski, and K. Ulaczyk, The Astrophysical Journal **870**, L10 (2019), URL `https://doi.org/10.3847%2F2041-8213%2Faaf73f`.

[49] A.-C. Eilers, D. W. Hogg, H.-W. Rix, and M. K. Ness, The Astrophysical Journal **871**, 120 (2019), URL `https://doi.org/10.3847%2F1538-4357%2Faaf648`.

[50] M. Maggiore, *Gravitational Waves. Vol. 1: Theory and Experiments*, Oxford Master Series in Physics (Oxford University Press, 2007), ISBN 978-0-19-857074-5, 978-0-19-852074-0.

[51] R. Abbott et al. (LIGO Scientific, VIRGO, KAGRA) (2022), 2204.04523.

[52] A. G. Suvorov, A. Mastrano, and U. Geppert, Monthly Notices of the Royal Astronomical Society **459**, 3407 (2016), ISSN 0035-8711, https://academic.oup.com/mnras/article-

pdf/459/3/3407/8110424/stw909.pdf, URL https://doi.org/10.1093/mnras/stw909.
[53] F. Gittins, N. Andersson, and D. I. Jones, Monthly Notices of the Royal Astronomical Society **500**, 5570 (2020), URL https://doi.org/10.1093%2Fmnras%2Fstaa3635.
[54] and R. Abuter, A. Amorim, M. Bauböck, J. P. Berger, H. Bonnet, W. Brandner, Y. Clé net, V. C. du Foresto, P. T. de Zeeuw, J. Dexter, et al., Astronomy & Astrophysics **625**, L10 (2019), URL https://doi.org/10.1051%2F0004-6361%2F201935656.
[55] V. Bozza and L. Mancini, Astrophys. J. **753**, 56 (2012), 1204.2103.
[56] K. Akiyama et al. (Event Horizon Telescope), Astrophys. J. Lett. **930**, L12 (2022).
[57] R. Abuter et al. (GRAVITY), Astron. Astrophys. **657**, L12 (2022), 2112.07478.
[58] P. Gondolo and J. Silk, Phys. Rev. Lett. **83**, 1719 (1999), astro-ph/9906391.
[59] L. Hui, J. P. Ostriker, S. Tremaine, and E. Witten, Phys. Rev. D **95**, 043541 (2017), 1610.08297.
[60] J. M. Ezquiaga and M. Zumalacárregui, Phys. Rev. D **102**, 124048 (2020), 2009.12187.
[61] S. Goyal, A. Vijaykumar, J. Ezquiaga, and M. Zumalacárregui (????), 2212.xxxxx.
[62] P. Schneider, J. Ehlers, and E. E. Falco, *Gravitational Lenses* (1992).
[63] T. Pyne and M. Birkinshaw, Astrophys. J. **415**, 459 (1993), astro-ph/9303020.
[64] S. Frittelli, Mon. Not. Roy. Astron. Soc. **340**, 457 (2003), astro-ph/0212207.
[65] R. Takahashi and N. Seto, Astrophys. J. **575**, 1030 (2002), arXiv:astro-ph/0204487.
[66] N. Seto, Mon. Not. Roy. Astron. Soc. **333**, 469 (2002), arXiv:astro-ph/0202364.
[67] R. E. Kass and A. E. Raftery, J. Am. Statist. Assoc. **90**, 773 (1995).
[68] J. S. Speagle, Monthly Notices of the Royal Astronomical Society **493**, 3132 (2020), URL https://doi.org/10.1093%2Fmnras%2Fstaa278.